

Article

Effects of Pressure on Microstructure and Residual Stresses during Hot Isostatic Pressing Post Treatment of AISI M50 Produced by Laser Powder-Bed Fusion

Siyuan Qin ^{*}, Simone Herzog , Anke Kaletsch  and Christoph Broeckmann

Institute for Materials Applications in Mechanical Engineering, RWTH Aachen University, 52064 Aachen, Germany; s.herzog@iwm.rwth-aachen.de (S.H.); a.kaletsch@iwm.rwth-aachen.de (A.K.); c.broeckmann@iwm.rwth-aachen.de (C.B.)

* Correspondence: s.qin@iwm.rwth-aachen.de; Tel.: +49-(0)241-809-9547

Abstract: Laser powder-bed fusion (LPBF) enables the production of difficult-to-machine materials with near-net shape and complex geometries. Components made of tool steels produced by LPBF, even using high preheating temperature, tend to show residual porosity, cracks, and high residual stresses. Hot isostatic pressing (HIP) is able to densify components and modify their microstructure. Moreover, compared to conventional heat treatment at ambient pressure, rapid cooling within the HIP vessel can alleviate thermal stresses, warping or cracking during quenching. In this study, the effects of isostatic pressure on microstructure evolution and residual stresses are investigated. Samples were produced by LPBF. Partly, they were conventionally heat treated by austenitizing, quenching, and tempering, partly using a HIP-device with an integrated quenching facility. The microstructure was characterized by optical microscopy, scanning electron microscopy employing energy-dispersive X-ray spectroscopy, and X-ray diffraction analysis. The results showed that besides the densification of the material to the porosity of 0.001%, HIP influenced the microstructure evolution by retarding recrystallization during austenitization due to the pressure and led to slight compressive residual stresses around 11 MPa on the surface of components.

Keywords: laser powder-bed fusion; AISI M50; hot isostatic pressing; post treatment; residual stresses



Citation: Qin, S.; Herzog, S.; Kaletsch, A.; Broeckmann, C. Effects of Pressure on Microstructure and Residual Stresses during Hot Isostatic Pressing Post Treatment of AISI M50 Produced by Laser Powder-Bed Fusion. *Metals* **2021**, *11*, 596. <https://doi.org/10.3390/met11040596>

Academic Editor: Wei Zhou

Received: 15 March 2021

Accepted: 1 April 2021

Published: 6 April 2021

Publisher's Note: MDPI stays neutral with regard to jurisdictional claims in published maps and institutional affiliations.



Copyright: © 2021 by the authors. Licensee MDPI, Basel, Switzerland. This article is an open access article distributed under the terms and conditions of the Creative Commons Attribution (CC BY) license (<https://creativecommons.org/licenses/by/4.0/>).

1. Introduction

Additive manufacturing (AM), also known as 3D-printing, describes technologies to fabricate three dimensional parts directly from computer-aided designed models [1]. Laser powder-bed fusion (LPBF) is a layer-wise AM technology that utilizes a high-power laser to consolidate metallic powders [2]. This process has the potential to fabricate tools or dies due to its capability of producing parts with complex geometry, for instance, internal cooling channel [3].

The characteristics of the LPBF thermal profile are rapid heating and cooling. Most of the lower layers experience reheating and remelting. Residual stress from this distinctive thermal profile leads to geometrical distortion and can negatively affect mechanical properties [4,5]. Decreasing the temperature gradient between melt-pool and powder-bed by preheating the feedstock powder or the baseplate is the most common method to reduce residual stresses [6]. A post heat treatment of as-built parts is able to reduce 70% of residual stresses [7]. On the other hand, the quenching process also generates residual stresses due to the temperature difference in the component leading to location- and time-dependent phase transformation [8].

Various grades of alloys have been used for the LPBF process, such as steels, titanium alloys, aluminum alloys, and nickel-based alloys [2]. Only a few pieces of research on tool steels have been published. These investigations concentrate on hot work steel AISI H13 and high speed steel AISI M2 [9,10]. AISI M50 (DIN 1.3551), which presents high

hot hardness due to molybdenum carbides, is used as bearings for turbine engines [11]. The high alloyed, martensitic steel AISI M50 can be used for ball bearings as well as for highly loaded tools. Conventionally heat-treated M50 presents MC and M₂C carbides and the morphology of martensitic matrix depends on the austenitizing temperature [12,13]. Recently, this tool steel was successfully processed by LPBF [14]. Kunz et al. characterized the microstructure of LPBF samples produced with different preheating temperatures and compared mechanical properties of the specimens produced conventionally or by LPBF [15,16].

Hot isostatic pressing (HIP), as a pressurized heat treatment process, can effectively reduce the porosity of parts fabricated via additive manufacturing [15]. Meanwhile, industrial equipment is available, which integrates a rapid quenching process into a HIP unit and allows for simultaneous pore densification and heat treatment. This is particularly beneficial in achieving the desired microstructure as well as decreasing the overall time of heat treatment [17]. The current studies about the influence of HIP with rapid cooling can be divided into two aspects. Firstly, the high pressure stabilizes the close packed austenitic crystal structure, which influences the kinetics of phase transformation. Lower temperatures and longer time are necessary for the transformation from γ -Fe to α -Fe [18,19]. Secondly, the quenching rate inside the HIP vessel is higher than inside a vacuum furnace [20]. However, the effects of HIP on austenitization have been seldomly studied.

Here, we study the influence of pressure on the heat treatment of AISI M50 produced by LPBF, by using a HIP unit with integrated quenching for postprocessing of the samples. The microstructure evolution was characterized and the influence of post treatments on residual stresses was evaluated. We also discuss the effects of pressure on the austenitization process by the application of the parent austenite reconstruction method.

2. Materials and Methods

The AISI M50 powder was atomized under the argon atmosphere in an EIGA plant by Nanoval GmbH & Co. KG (Berlin, Germany). The M50 powder was mainly spherical and exposed d₁₀, d₅₀, and d₉₀ values of 16, 25, and 36 μ m, respectively. In Table 1, the ASTM chemical compositions of M50 [21] and M50 powder used in this study are compared. Obviously, the chemical composition of the M50 powder lies in the specified range.

Table 1. Standard chemical composition of M50 (ASTM A600-92a [21]) and the chemical composition of M50 powder in this study.

	Elements [Mass%]					
	Fe	C	Cr	Mo	V	Mn
ASTM	Bal.	0.78–0.88	3.75–4.5	3.9–4.75	0.7–1.25	0.15–0.45
Laser Powder-Bed Fusion (LPBF) Powder	Bal.	0.84	4.49	4.53	1.03	0.31

2.1. Sample Production

Samples were produced by the ReaLizer SLM 100 machine (ReaLizer GmbH, Borcheln, Germany), under argon atmosphere. The machine contains the ytterbium fiber laser with a wavelength of 1070 nm and is equipped with a preheating device that heats the bottom of the powder bed. Optimal process parameters with minimized porosity were found with a laser power of 160 W, a laser speed of 1 m/s, and a hatch distance of 100 μ m. The layer thickness was 30 μ m. Two groups of samples were built at two different preheating temperatures, 250 and 500 °C. Cubic samples in the dimension of 10 mm \times 10 mm \times 10 mm were produced for residual stress measurement and rectangular samples with the dimension of 10 mm \times 5 mm \times 5 mm were produced for dilatometry tests.

2.2. Thermodynamic Calculation

The thermodynamic calculation was carried out by Thermo-Calc software (2020a, Thermo-Calc Software, Solna, Sweden) with the TCFE9 database for the AISI M50 powder

composition under a pressure of 1.0 bar. The Ac3 temperature was 818 °C, according to the calculated diagram (Figure 1). The austenitization temperature of conventional heat treatment and HIP temperature was chosen as 1200 °C, where all types of carbides were solved to ensure a complete austenitization. At 580 °C, a large fraction of carbides was visible. These carbides in M50 steel can be used to increase hardness as well as toughness by secondary hardening. Therefore, tempering was performed at 580 °C in this study.

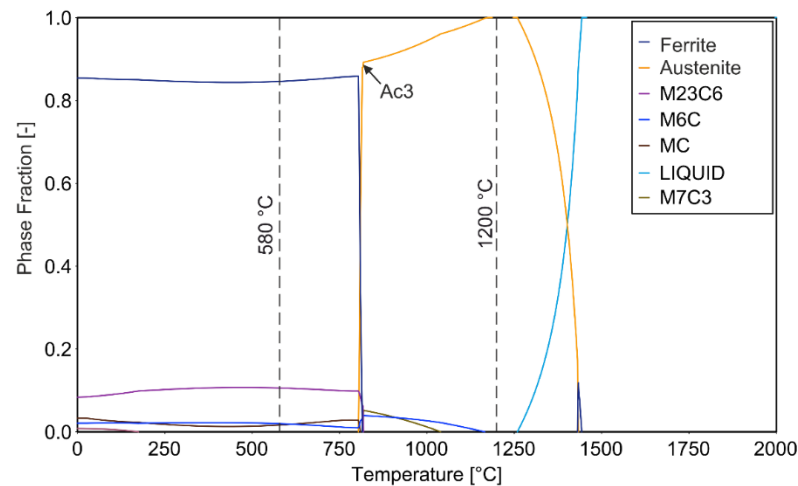


Figure 1. Calculated equilibrium phase fraction of the M50 powder.

2.3. Post Treatment

After additive manufacturing by LPBF, two variants of post treatments were investigated in this study. A series of the samples was heat treated conventionally at Dörrenberg Edelstahl GmbH (Engelskirchen-Ruenderoth, Germany) (Figure 2a). Specifically, the samples were austenitized at 1200 °C for 20 min in a vacuum furnace followed by nitrogen gas quenching with 5 bar. Subsequent triple tempering was performed at 580 °C for 3.5 h each in a vacuum furnace.

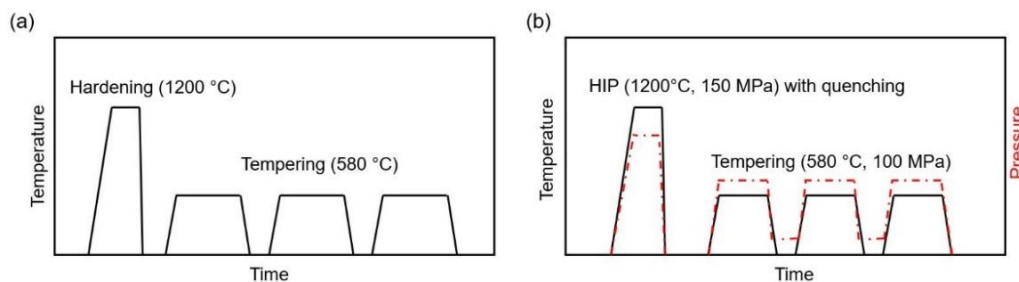


Figure 2. Schematic diagram of post treatments: (a) conventional heat treatment; (b) hot isostatic pressing (HIP) integrated with quenching and tempering.

The second series of the samples was hot isostatically pressed using a Uniform Rapid Quenching (URQ) furnace under argon process gas at the Quintus Technologies Application Centre (Västerås, Sweden) (Figure 2b). The HIP process went through a similar thermal profile to the conventional heat treatment: the HIP temperature of 1200 °C was held at 150 MPa for 20 min followed by gas cooling and triple tempering at 580 °C and 100 MPa for 3 h each.

2.4. Dilatometry

Since the quenching rate in the conventional heat treatment was lower than in the HIP process and the thermal profile of conventional heat treatment was not exactly the same as

during the HIP process, dilatometry tests were performed as the control group in order to study the influence of pressure on microstructure.

The samples were tested by the dilatometer DIL805 A/D/T (TA Instruments, New Castle, DE, USA). Two samples were austenitized for 20 min at 1200 °C in vacuum, followed by argon quenching and triple tempering at 580 °C for 3 h each. After testing, the microstructure was analyzed by optical microscopy and scanning electron microscope (SEM) investigations of the cross section. Figure 3 presents the cooling rate of HIP unit and dilatometer, determined at the sample surface.

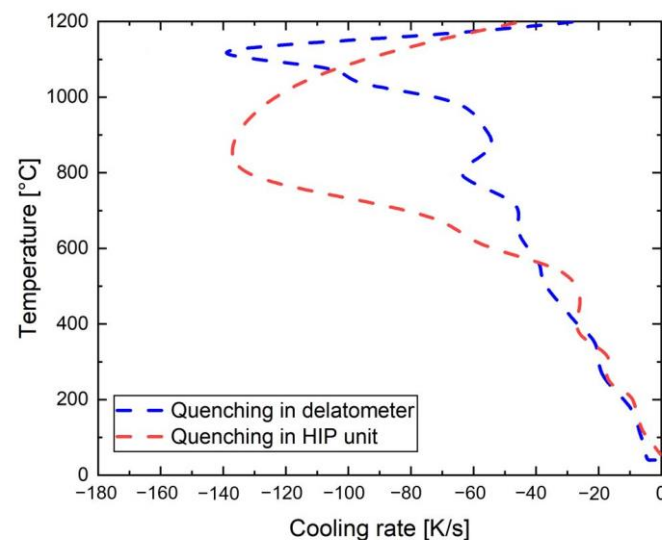


Figure 3. Cooling rate in dilatometer and HIP unit.

2.5. Microstructure

The microstructure was characterized in as-built and post-treated conditions. Samples were cut along the building direction and prepared by standard metallographic techniques with a finishing step of mechanical polishing using colloidal silica suspension. The porosity was determined by unetched sections with the magnitude of 100× by image analysis. Ten sections at random positions for each sample were analyzed. The majority of pores were spherical and only the percentage of porosity was analyzed. For the microstructure characterization, prepared samples were etched by V2A reagent for 10 s. The microstructural analysis was observed by an optical microscope and the scanning electron microscope Helios Nanolab G3 CX (FEL, Hillsboro, OR, USA) assembled with Secondary Electron (SE), Energy-Dispersive X-ray Spectroscopy (EDS), and Electron Backscatter Diffraction (EBSD) detectors. EBSD was performed with a step size of 50 nm using an acceleration voltage of 15 kV. The TSL OIM Analysis™ software (7.3.1, EDAX Inc, Mahwah, NJ, USA) was used for EBSD data analysis.

The ARPGE software was used to reconstruct the parent austenite grains from the EBSD data [22]. An algorithm, which calculates the orientation relationship between the γ -Fe and α' -Fe, was applied to identify the variants that are directly inherited by a single parent austenite grain. When the misorientation of two reconstructed parent grains is lower than 2°, they are considered as one grain. The Kurdjumov–Sachs (K–S) relationship between parent austenite and martensite ($\{111\}_{\gamma} // \{011\}_{\alpha'}$, $\langle \bar{1}01 \rangle_{\gamma} // \langle \bar{1}\bar{1}1 \rangle_{\alpha'}$) was used for the reconstruction. In the K–S orientation relationship, there are 24 variants when the crystallography symmetry is considered.

2.6. Residual Stress Measurement

The X-ray Diffraction System 3003 PTS (GE Inspection Technologies, New York, NY, USA) with a Cr X-ray tube was applied for the XRD phase analyses and the residual stress measurement. The intensity distribution of Cr-K α X-rays, scattered from M50 samples,

was recorded in the measuring range of $60^\circ \leq 2\theta \leq 165^\circ$ with a counting time of 10 s in steps of 0.05° . The respective X-ray pattern was characterized and analyzed by Materials Analysis Using Diffraction (MAUD) software (2.91 version) for phase analysis (ICDD/PDF 00-006-0696 for ferrite and ICDD/PDF 00-023-0298 for austenite). The Fe-bcc {211} peak at $2\theta \approx 156.08^\circ$ was selected to analyze residual stresses. The residual stresses were determined by the $\sin^2\psi$ method.

3. Results

3.1. Porosity

M50 cubic samples were produced without any visible cracks or delamination at the preheating temperature 250 and 500 °C with the relative porosity of 0.08 and 0.04%, respectively. Figure 4 presents the porosity of the samples in different conditions. The sample fabricated at 500 °C preheating temperature was conventionally heat treated and showed a porosity of 0.04%. After HIP process, almost no pore in the sample with the preheating of 500 °C could be detected by optical microscope and the corresponding porosity was 0.001%.

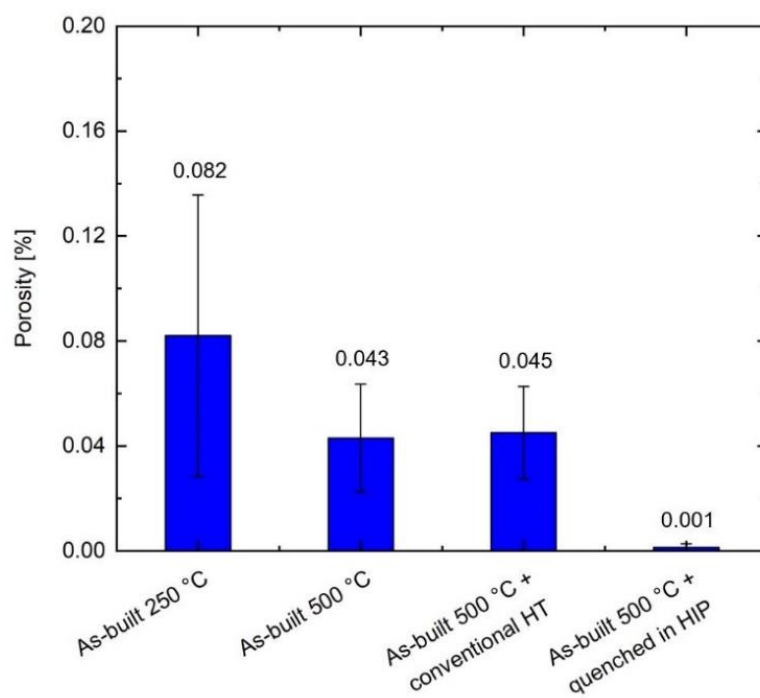


Figure 4. Porosity (middle value and standard deviation) in different conditions. For the two post treatments, samples built with preheating at 500 °C were used.

3.2. Microstructure Evolution

The optical micrographs of the as-built samples in Figure 5a,b show the characteristics of material produced by LPBF. Through the distinct laser tracks, the layer development of LPBF process is able to be clearly identified after etching. The grains grew epitaxially along the building direction due to the thermal gradient. Figure 5c shows the microstructure (preheating temperature 500 °C) after hardening and tempering, referred as conventional heat treatment in this study. Needle-like martensitic structures were observed in matrix and the layerwise structure from LPBF process was eliminated. A similar acicular martensitic matrix is observed in Figure 5d, where the microstructure after HIP with integrated quenching and tempering (preheating temperature 500 °C) is presented. These two post treatments were performed at the same austenitization and tempering temperature and led to similar martensitic microstructures.

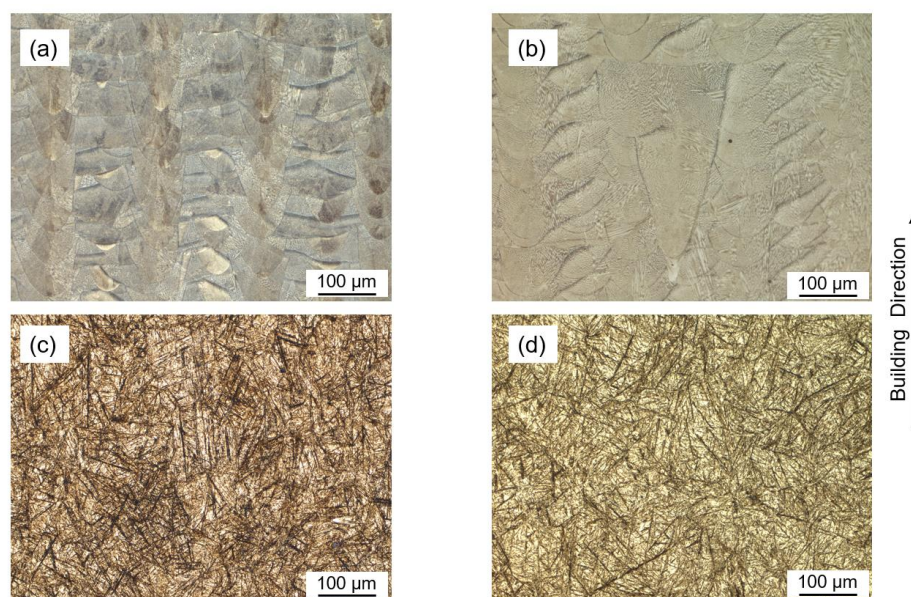


Figure 5. Optical micrographs: (a) as-built with a preheating of 250 °C; (b) as-built with a preheating of 500 °C; (c) conventional heat treatment; (d) HIP integrated with quenching and tempering.

Carbides can be observed with higher magnification by SEM. Figure 6a shows the microstructure of an as-built sample at the preheating temperature 250 °C. Carbon enriched area was combined as a cellular network-shape because of the rapid cooling of melting pools. During the subsequent heat treatment, hardening, and tempering, these carbon atoms during austenitization were solved in the matrix. During tempering, reprecipitation formed spherical secondary carbides in the size of 100 nm, homogeneously distributed within the martensite (Figure 6b). A similar microstructure was presented in the heat treated sample produced with the preheating temperature of 500 °C. After HIP with integrated quenching, no carbides can be observed by SEM and the martensite appears plate-like shape (Figure 6c). Similar to the conventional heat treatment, spherical carbides, likely Mo rich M_2C and V rich MC as described in [12], were dispersed in the matrix after tempering in the HIP unit (Figure 6d).

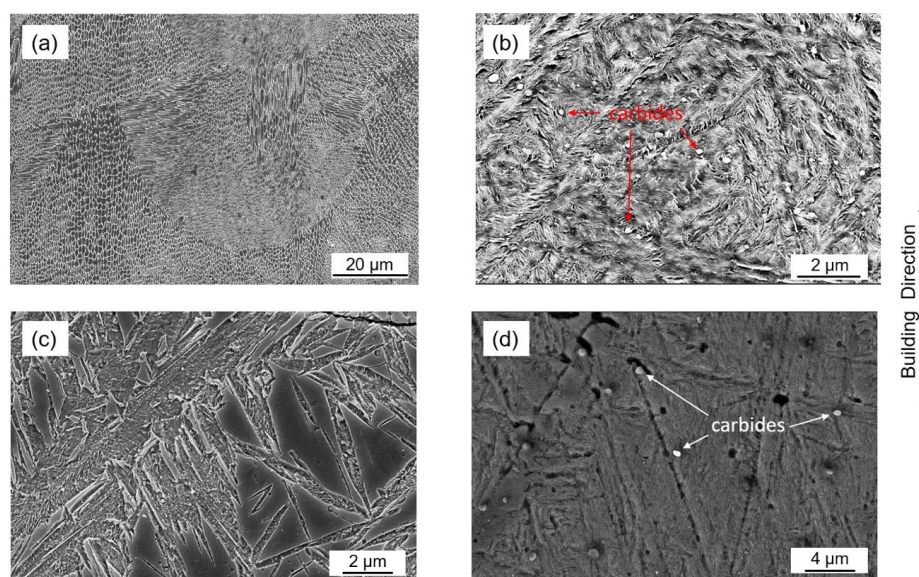


Figure 6. SEM images of microstructure. (a) as-built with 250 °C preheating; (b) conventional heat treatment; (c) HIP with quenching; (d) HIP with quenching and tempering.

Elemental mapping revealed an inhomogeneous element distribution. Figure 7 shows the microstructure of the as-built sample with 250 °C preheating and corresponding EDS mappings. The fast solidification of the melting pool during the LPBF process led to the segregation of alloy elements. The cellular walls were enriched with carbon and carbides forming elements like Cr, Mo, and V.

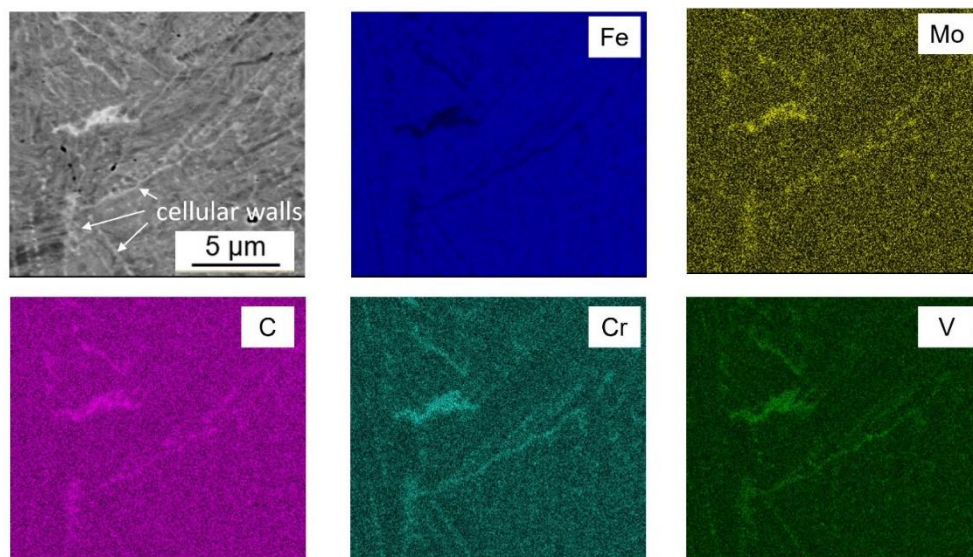


Figure 7. Backscattered-Electron (BSE) micrograph of the as-built sample with 250 °C preheating temperature and corresponding elemental Energy Dispersive Spectroscopy (EDS) mapping.

Figure 8 presents the result of the EBSD measurement of the sample produced at the preheating temperature of 250 °C. In the EBSD phase map (Figure 8a), a small amount of retained austenite remains among the martensitic dendrites. The white area was supposed to be the carbon enriched area, which cannot be indexed by EBSD measurement. A fine martensite microstructure could be identified by the Inverse Pole Figure (IPF) (Figure 8b), which illustrated the crystal orientation of grains. The dendrites elongated in building direction with similar grain orientation.

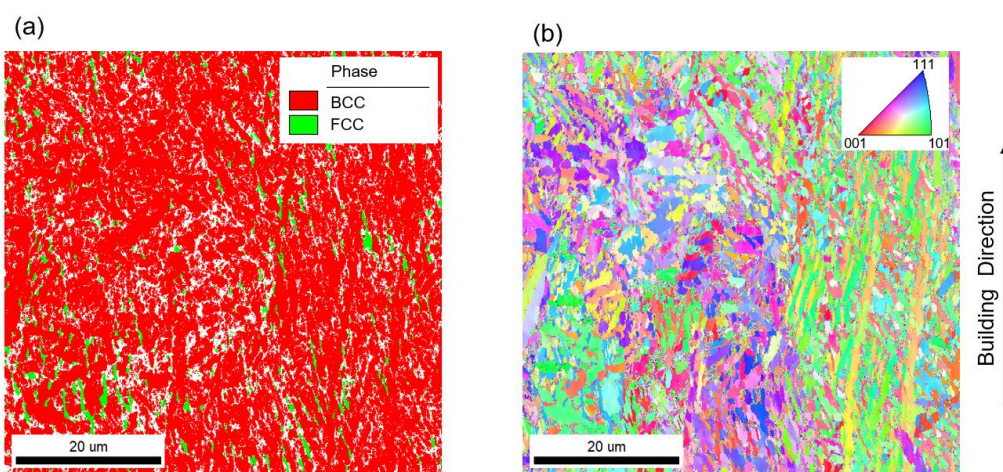


Figure 8. Electron Backscatter Diffraction (EBSD) phase map (a) and inverse pole figure map (b) of as-built sample produced at 250 °C.

More insights into the phase evolution can be obtained by XRD diffraction patterns, depicted in Figure 9. In as-built condition, both fcc and bcc phases were present. The fcc

peaks indicated the presence of retained austenite. Whereas, the bcc peaks represented martensite as well as bainite, since both consisted of a distorted bcc lattice structure. After HIP and quenching, martensite formed from austenite. Retained austenite can also be detected in the sample. During three sessions of tempering, this retained austenite fully transformed into martensite, since no fcc diffraction peak can be detected. The samples conventionally heat treated present a similar diffraction pattern. After hardening and tempering, most of the matrix is martensite with less than 5% retained austenite. Theoretically, the high pressure (150 MPa) in the HIP furnace should decrease the martensite start temperature by around 15 K according to the Clausius–Clapeyron equation [20]. This should result in a higher content of retained austenite. Nonetheless, this slight difference could not be observed from microstructure and XRD pattern since the cooling conditions were different in both furnaces: The cooling rate was higher in the HIP furnace than in the vacuum furnace.

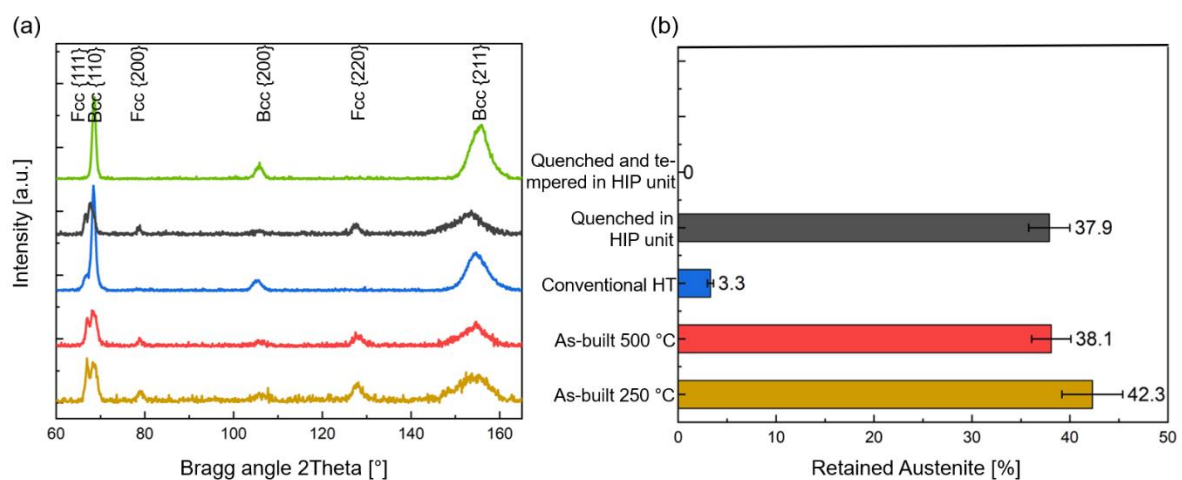


Figure 9. (a) XRD phase diffraction pattern and (b) retained austenite fraction in different conditions.

3.3. Parent Austenite Reconstruction

The samples from preheating at 500 °C were austenitized and quenched either inside the HIP furnace or using the dilatometer through the same thermal profile. The most significant difference between these two post-treatment methods is that inside the HIP furnace a hydrostatic pressure was applied. The corresponding microstructures were analyzed by EBSD.

Figure 10a presents the microstructure and grain orientation of the material that was densified and quenched in the HIP furnace by IPF map. Fine martensitic plates formed during the quenching process. The reconstructed parent austenite grains that were based on the K–S orientation relationship by ARPGE software are shown in Figure 10b. These austenite grains were recrystallized during the annealing process from the as-built microstructure. The misorientation distribution profile of martensitic blocks/plates on the AB line in Figure 10a was measured, as shown in Figure 10c, which illustrates the fine martensitic plates in the microstructure. The width distribution of martensitic plates is presented in Figure 10d.

Figure 11 shows the microstructure characteristics of the sample annealed and quenched in the dilatometer. Relative coarse martensite microstructure can be observed in Figure 11a. Figure 11b presents the parent austenite of the martensite before quenching. The misorientation profile (Figure 11c) along line AB illustrates the width of martensitic blocks/plates. Figure 11d shows the width distribution of martensitic plate. Coarser martensitic blocks/plates were formed, compared with the sample quenched inside of the HIP furnace.

3.4. Residual Stresses

Figure 12 shows the surface residual stresses of samples in different conditions. The residual stresses were measured at the center of a side surface of cubic samples ($10\text{ mm} \times 10\text{ mm} \times 10\text{ mm}$) in building direction and transverse direction after removing the samples from the support structure.

Both as-built samples present compressive residual stresses in building direction. In the transverse direction, the as-built sample processed with a preheating temperature of $500\text{ }^\circ\text{C}$ shows a slight compressive stress of 9 MPa , whereas, tensile stress of 55 MPa was obtained in the sample produced at $250\text{ }^\circ\text{C}$.

During the conventional heat treatment, tensile residual stresses were generated by the quenching process, and they were not fully relieved by the subsequent tempering. Tensile stresses were 48 MPa in building direction and 44 MPa in transverse direction after the whole heat treatment. The sample, quenched in a HIP furnace under high pressure, presented compressive stresses (99 MPa in building direction and 14 MPa in transverse direction).

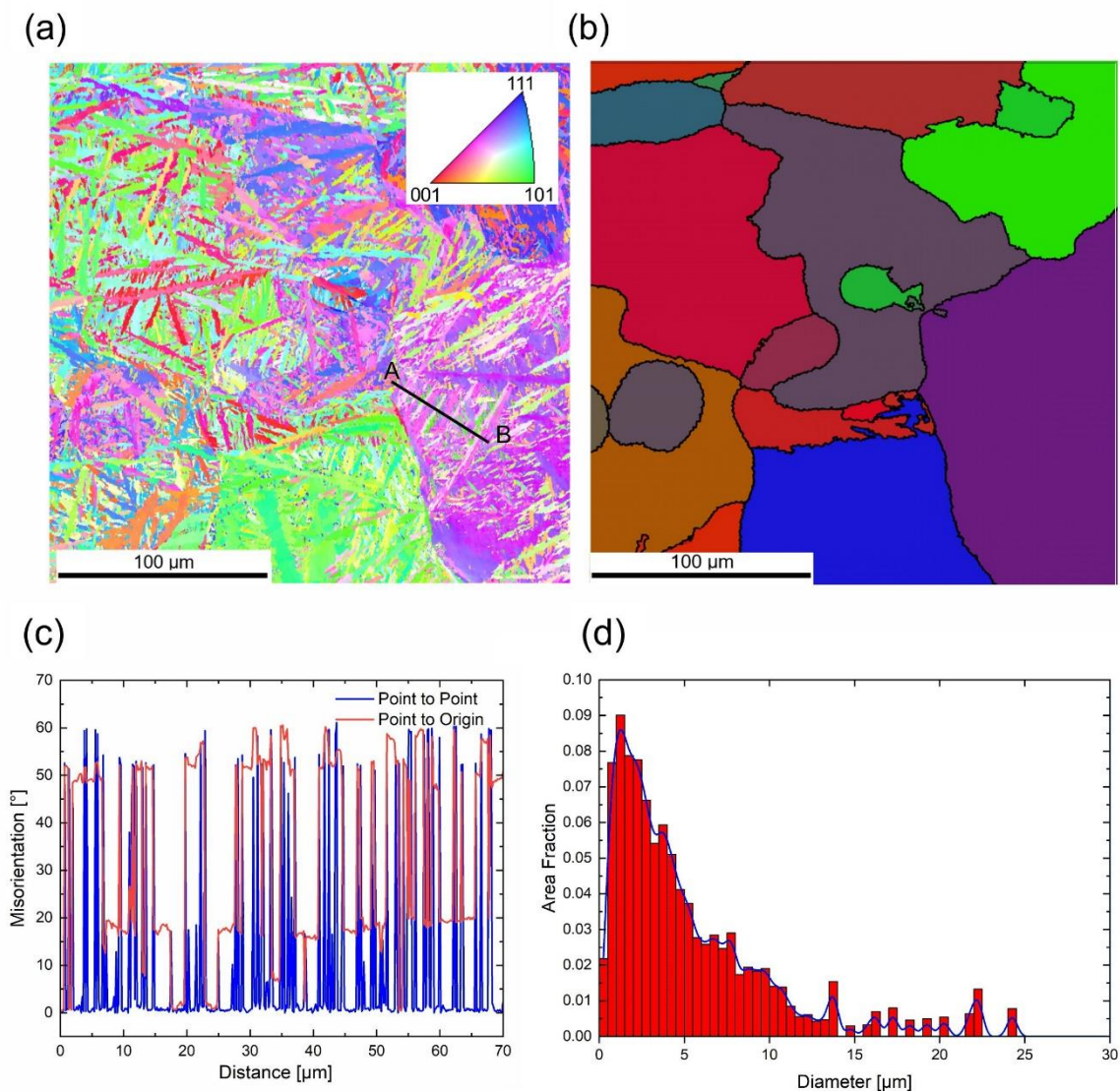


Figure 10. Microstructure analysis of the sample annealed and quenched in the HIP furnace. (a) An Inverse Pole Figure (IPF) map features the fine martensitic plates. (b) The corresponding parent austenite grains are reconstructed based on the EBSD result. (c) Point-to-point and point-to-origin misorientation profile of AB line in (a), which illustrates the width of martensite plates/blocks. (d) Martensitic plate width distribution.

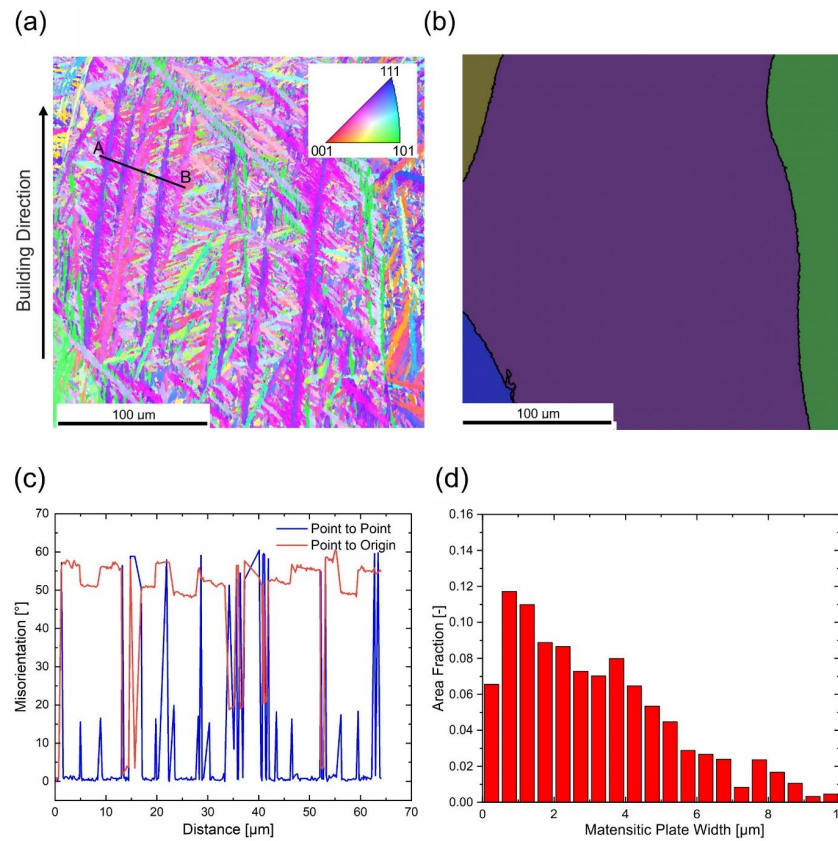


Figure 11. Microstructure analysis of the sample annealed and quenched in dilatometer. (a) Relative coarse martensite is presented by the IPF map. (b) The corresponding parent austenite is reconstructed based on EBSD result. (c) Point-to-point and point-to-origin misorientation profile of AB line in (a). (d) Martensitic plate width distribution.

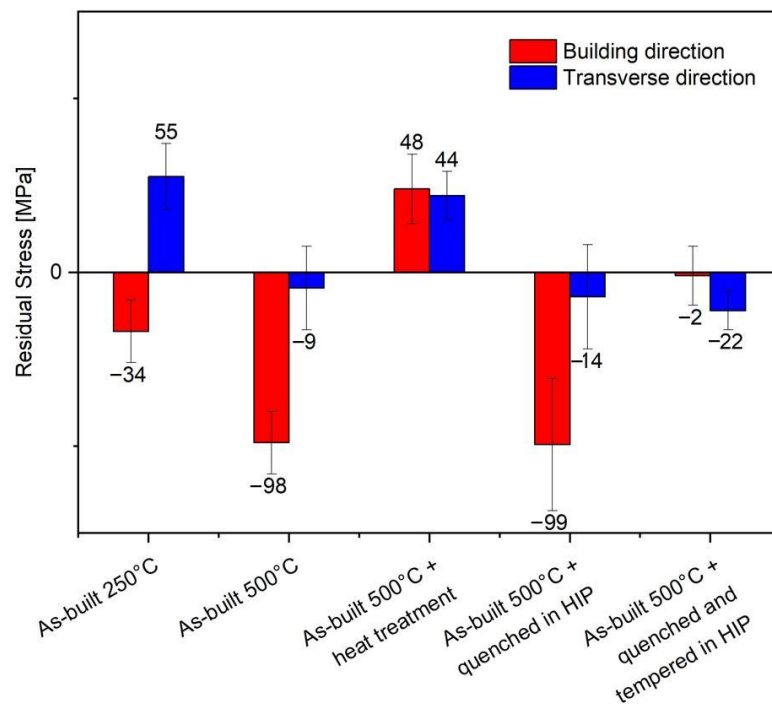


Figure 12. Residual stresses in different conditions.

4. Discussion

4.1. Influence of LPBF Preheating Temperature on Microstructure

In as-built condition, the samples produced with higher preheating temperature contained fewer pores. As for the microstructure, there is no significant difference between the two selected preheating temperatures. However, the XRD results illustrated a lower retained austenite content in the samples fabricated with the higher preheating temperature. For tool steel H13, similar observations were reported [23]. At higher preheating temperature, carbon solid solution atoms tended to precipitate from the supersaturated matrix. The martensitic/bainitic transformation caused strong elastic lattice distortions, which naturally counteract the transformation. Additionally, with low carbon content in matrix, these distortions can be reduced by gliding and recovery mechanisms. Therefore, the higher preheating temperature leads to a lower volume fraction of retained austenite after the gamma-to-alpha phase transformation. Based on the M50 continuous cooling transformation diagram reported by Kunz et al. [15], the martensitic transformation start temperature was about 200 °C and bainite was formed between 200 and 400 °C. Therefore, it can be concluded that bainite is contained in XRD diffraction bcc peaks of both as-built samples.

4.2. Effects of HIP with Integrated with Quenching

Pores in the components fabricated by LPBF had a deleterious effect on the mechanical properties and influences the fracture micromechanisms [24]. For instance, fatigue strength of samples manufactured by LPBF was strongly affected by the porosity, since fatigue cracks initiate from pores [25]. Toughness can be improved by the enclosure of pores [26,27]. Furthermore, pores within additively manufactured parts reduced the corrosion resistance considerably [28]. Therefore, the reduction of porosity and pore size was of great importance to improve the properties of parts processed by LPBF. HIP was considered as one feasible solution to reduce closed porosity. The applied pressure by inert gas led to the densification of material by plastic flow and material transport, which was utilized for the bonding process as well [29]. Figure 4 presents the porosity of M50 parts in different conditions. After HIP, porosity was reduced pronouncedly in comparison to the conventional heat treatment.

Moreover, HIP also influenced the microstructure. Most previous studies focused on the gamma to alpha phase transformation process. The high pressure inside the HIP furnace shifted this phase transformation to lower temperature and longer time [18]. On the other hand, high cooling rates in the HIP furnace by compressed gas contributed to the martensitic transformation [20]. As no significant differences of the microstructure between the samples heat treated conventionally or within the HIP furnace can be observed in this study by light optical microscope, both effects either compensated each other or were only less pronounced at the pressure level used by HIP.

In addition, the effects of hydrostatic pressure on recrystallization during austenitization should not be neglected. The sample austenitized in the dilatometer at ambient pressure showed coarser parent austenite grains than the one annealed under pressure in the HIP furnace (Figures 10b and 11b). The hydrostatic pressure during annealing slowed down the diffusion processes by an increase of the activation energy for diffusion. As a result, recrystallization and grain growth were retarded [30,31]. Hence, annealing in a HIP furnace with high hydrostatic pressure led to finer austenite grains, compared to annealing in vacuum. Furthermore, martensitic block width and packet size were proportional to the prior austenite grain size, that is, small austenite grains resulted in fine martensitic structure [32,33]. This explained why the martensitic structure appeared finer after quenching under pressure in the HIP furnace than by quenching pressureless in a dilatometer, even though they share similar cooling rates. To sum up, hydrostatic pressure by HIP in a magnitude of 150 MPa caused finer microstructure since the pressure retards the recrystallization process.

4.3. Residual Stresses

The temperature gradient mechanism (TGM) model was used to explain the formation of residual stress for the LPBF process (Figure 13) [4,6]. During the heat stage, the laser source heated up the top layer rapidly. The heated area tended to expand, but was constrained by the surrounding material. Therefore, the heat affected zone formed compressive stresses. If the compressive stress exceeded the yield stress of material, it would be partially relieved by plastic deformation. During the cooling stage, the previously heated area started to cool down and shrink. This shrinkage led to tensile residual stresses. This simplified model was not capable of explaining or predicting the residual stresses generated from complex thermal LPBF cycles. Moreover, density changes due to phase transformations during cooling were not considered in this model. However, the model provided a good explanation that, with lower preheating temperature, the residual stress tends to transfer from compression to tension due to the higher thermal gradient during the cooling stage.

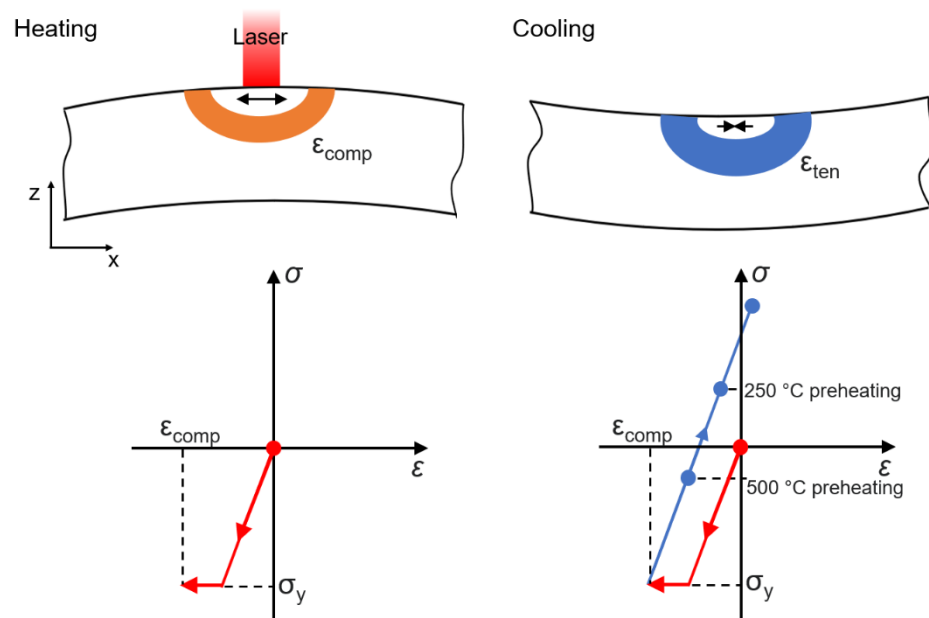


Figure 13. Schematic illustration of temperature gradient mechanism (TGM) model, according to [6].

The magnitude of the residual stresses caused by the LPBF process was limited by the yield limit of the material at room temperature. The residual stresses can be partially relieved during successive heat treatment by plastic yield due to the reduced yield limit at elevated temperature. Even though both post treatments investigated in this study went through a similar thermal history, high pressure seemed to support slight compressive residual stresses after tempering in the HIP furnace. Depending on the application, a state of surface compressive residual stresses was beneficial, for instance to increase life under fatigue loading conditions.

5. Conclusions

In this study, the effect of pressure during HIP post treatment with integrated quenching on the microstructure evolution and residual stresses of high alloyed steel AISI M50 fabricated by LPBF was analyzed.

Using a preheating temperature of 500 °C, LPBF led to a lower retained austenite fraction, compared to 250 °C preheating. Cellular network-shaped carbon segregation areas could be observed in both as-built conditions. After quenching, plate-like martensite formed in the matrix. During tempering, retained austenite transformed to martensite and fine Mo and V-rich carbides precipitated.

High pressure of the HIP process retarded recrystallization and grain growth during austenitization, causing fine parent austenite grains, which led to small martensitic packet/block size after quenching.

A shift of residual stresses at the surface of as-built samples were observed, which tended to transform tensile stresses to compressive stresses at higher preheating temperature. A preheating temperature of 500 °C thus improved the state of near surface residual stresses in as-built components made of M50 steel. Integrated heat treatment in a HIP furnace ended up in small compressive residual stresses, whereas, conventional heat treatment led to tensile residual stresses at the surface of the samples.

Author Contributions: Conceptualization, S.Q., S.H., A.K., and C.B.; methodology, S.Q.; formal analysis, S.Q.; investigation, S.Q.; resources, C.B.; writing—original draft preparation, S.Q.; writing—review and editing, S.Q., S.H., A.K., and C.B.; visualization, S.Q.; supervision, A.K. and C.B. All authors have read and agreed to the published version of the manuscript.

Funding: This research was funded by Deutsche Forschungsgemeinschaft (DFG, German Research Foundation) under Germany's Excellence Strategy—EXC-2023 Internet of Production, grant number 390621612.

Data Availability Statement: The data presented in this study are available on request from the corresponding author. The data are not publicly available because they are part of an ongoing study.

Acknowledgments: The authors would like to thank Quintus Technologies Application Centre and Dörrenberg Edelstahl GmbH for performing the post treatments. This study was funded by the Deutsche Forschungsgemeinschaft (DFG, German Research Foundation) under Germany's Excellence Strategy—EXC-2023 Internet of Production—390621612.

Conflicts of Interest: The authors declare no conflict of interest.

References

1. Sames, W.J.; List, F.A.; Pannala, S.; Dehoff, R.R.; Babu, S.S. The metallurgy and processing science of metal additive manufacturing. *Int. Mater. Rev.* **2016**, *61*, 315–360. [[CrossRef](#)]
2. Frazier, W.E. Metal Additive Manufacturing: A Review. *J. Mater. Eng. Perform.* **2014**, *23*, 1917–1928. [[CrossRef](#)]
3. Casati, R.; Coduri, M.; Lecis, N.; Andrianopoli, C.; Vedani, M. Microstructure and mechanical behavior of hot-work tool steels processed by Selective Laser Melting. *Mater. Charact.* **2018**, *137*, 50–57. [[CrossRef](#)]
4. Mercelis, P.; Kruth, J. Residual stresses in selective laser sintering and selective laser melting. *Rapid Prototyp. J.* **2006**, *12*, 254–265. [[CrossRef](#)]
5. Yan, J.J.; Zheng, D.L.; Li, H.X.; Jia, X.; Sun, J.F.; Li, Y.L.; Qian, M.; Yan, M. Selective laser melting of H13: Microstructure and residual stress. *J. Mater. Sci.* **2017**, *52*, 12476–12485. [[CrossRef](#)]
6. Li, C.; Liu, Z.; Fang, X.; Guo, Y. Residual Stress in Metal Additive Manufacturing. *Procedia CIRP* **2018**, *71*, 348–353. [[CrossRef](#)]
7. Shiomi, M.; Osakada, K.; Nakamura, K.; Yamashita, T.; Abe, F. Residual Stress within Metallic Model Made by Selective Laser Melting Process. *CIRP Ann.* **2004**, *53*, 195–198. [[CrossRef](#)]
8. Soomro, A.B. The Generation of Thermal Stress and Strain during Quenching. Ph.D. Thesis, Sheffield Hallam University, Sheffield, UK, 2017.
9. Herzog, D.; Seyda, V.; Wycisk, E.; Emmelmann, C. Additive manufacturing of metals. *Acta Mater.* **2016**, *117*, 371–392. [[CrossRef](#)]
10. Yap, C.Y.; Chua, C.K.; Dong, Z.; Liu, Z.H.; Zhang, D.Q.; Loh, L.E.; Sing, S.L. Review of selective laser melting: Materials and applications. *Appl. Phys. Rev.* **2015**, *2*, 041101. [[CrossRef](#)]
11. Essa, F.; Zhang, Q.; Huang, X.; Ibrahim, A.M.M.; Ali, M.K.A.; Sharshir, S. Enhancing the tribological and mechanical properties of M50 steel using solid lubricants—A detailed review. *Proc. Inst. Mech. Eng. Part J J. Eng. Tribol.* **2017**, *232*, 619–642. [[CrossRef](#)]
12. Bridge, J.E.; Maniar, G.N.; Philip, T.V. Carbides in M-50 high speed steel. *Met. Mater. Trans. A* **1971**, *2*, 2209–2214. [[CrossRef](#)]
13. Iqbal, A.; Baig, M.S. Heat Treatment Response of Triple and Quintuple Tempered M50 High Speed Steel. *Eur. J. Sci. Res.* **2017**, *17*, 150–159.
14. Saewe, J.; Gayer, C.; Vogelpoth, A.; Schleifenbaum, J.H. Feasibility Investigation for Laser Powder Bed Fusion of High-Speed Steel AISI M50 with Base Preheating System. *BHM Berg. Hüttenmännische Mon.* **2019**, *164*, 101–107. [[CrossRef](#)]
15. Kunz, J.; Saewe, J.; Herzog, S.; Kaletsch, A.; Schleifenbaum, J.H.; Broeckmann, C. Mechanical Properties of High-Speed Steel AISI M50 Produced by Laser Powder Bed Fusion. *Steel Res. Int.* **2019**, *91*. [[CrossRef](#)]
16. Kunz, J.; Saewe, J.; Herzog, S.; Kaletsch, A.; Schleifenbaum, J.H.; Broeckmann, C. Influence of Powder Bed Temperature on Microstructure and Post Heat Treatment of High Speed Steel AISI M50 Processed by Laser Powder Bed Fusion. In Proceedings of the Euro PM 2018 Congress & Exhibition, Bilbao, Spain, 14–18 October 2018.

17. Weddeling, A.; Theisen, W. Energy and time saving processing: A combination of hot isostatic pressing and heat treatment. *Met. Powder Rep.* **2017**, *72*, 345–348. [[CrossRef](#)]
18. Fujita, M.; Suzuki, M. The Effect of High Pressure on the Isothermal Transformation in High Purity Fe-C Alloys and Commercial Steels. *Trans. Iron Steel Inst. Jpn.* **1974**, *14*, 44–53. [[CrossRef](#)]
19. Angré, A.; Ahlfors, M.; Chasoglou, D.; Larsson, L.; Claesson, E.; Karlsson, O. Phase transformation under isostatic pressure in HIP. *Powder Met.* **2017**, *60*, 1–8. [[CrossRef](#)]
20. Weddeling, A.; Wulbieter, N.; Theisen, W. Densifying and hardening of martensitic steel powders in HIP units providing high cooling rates. *Powder Met.* **2016**, *59*, 1–11. [[CrossRef](#)]
21. ASTM A600-92a. *Specification for Tool Steel High Speed*; ASTM International: West Conshohocken, PA, USA, 2016.
22. Cayron, C. ARPGE: A computer program to automatically reconstruct the parent grains from electron backscatter diffraction data. *J. Appl. Crystallogr.* **2007**, *40*, 1183–1188. [[CrossRef](#)]
23. Mertens, R.; Vrancken, B.; Holmstock, N.; Kinds, Y.; Kruth, J.-P.; Van Humbeeck, J. Influence of Powder Bed Preheating on Microstructure and Mechanical Properties of H13 Tool Steel SLM Parts. *Phys. Procedia* **2016**, *83*, 882–890. [[CrossRef](#)]
24. Konovalenko, I.; Maruschak, P.; Prentkovskis, O. Automated Method for Fractographic Analysis of Shape and Size of Dimples on Fracture Surface of High-Strength Titanium Alloys. *Metals* **2018**, *8*, 161. [[CrossRef](#)]
25. Le, V.-D.; Pessard, E.; Morel, F.; Edy, F. Influence of porosity on the fatigue behaviour of additively fabricated TA6V alloys. *MATEC Web Conf.* **2018**, *165*, 02008. [[CrossRef](#)]
26. Girelli, L.; Giovagnoli, M.; Tocci, M.; Pola, A.; Fortini, A.; Merlin, M.; La Vecchia, G.M. Evaluation of the impact behaviour of AlSi10Mg alloy produced using laser additive manufacturing. *Mater. Sci. Eng. A* **2019**, *748*, 38–51. [[CrossRef](#)]
27. Tekeli, S.; Güral, A. Microstructural characterization and impact toughness of intercritically annealed PM steels. *Mater. Sci. Eng. A* **2005**, *406*, 172–179. [[CrossRef](#)]
28. Sander, G.; Tan, J.; Balan, P.; Gharbi, O.; Feenstra, D.; Singer, L.; Thomas, S.; Kelly, R.; Scully, J.; Birbilis, N. Corrosion of Additively Manufactured Alloys: A Review. *Corrosion* **2018**, *74*, 1318–1350. [[CrossRef](#)]
29. AlHazaa, A.; Haneklaus, N. Diffusion Bonding and Transient Liquid Phase (TLP) Bonding of Type 304 and 316 Austenitic Stainless Steel—A Review of Similar and Dissimilar Material Joints. *Metals* **2020**, *10*, 613. [[CrossRef](#)]
30. Kühlein, W.; Stüwe, H. The influence of high hydrostatic pressure on recrystallization of α -brass. *Acta Met.* **1988**, *36*, 3055–3059. [[CrossRef](#)]
31. Krawczynska, A.T.; Gierlotka, S.; Suchecki, P.; Setman, D.; Adamczyk-Cieslak, B.; Lewandowska, M.; Zehetbauer, M. Recrystallization and grain growth of a nano/ultrafine structured austenitic stainless steel during annealing under high hydrostatic pressure. *J. Mater. Sci.* **2018**, *53*, 11823–11836. [[CrossRef](#)]
32. Maki, T.; Tsuzaki, K.; Tamura, I. The Morphology of Microstructure Composed of Lath Martensites in Steels. *Trans. Iron Steel Inst. Jpn.* **1980**, *20*, 207–214. [[CrossRef](#)]
33. Morito, S.; Saito, H.; Ogawa, T.; Furuhashi, T.; Maki, T. Effect of Austenite Grain Size on the Morphology and Crystallography of Lath Martensite in Low Carbon Steels. *ISIJ Int.* **2005**, *45*, 91–94. [[CrossRef](#)]